Ferroelectricity in boron-substituted aluminum nitride thin films

John Hayden,[1,*] Mohammad Delower Hossain,[1] Yihuang Xiong,[1] Kevin Ferri,[1] Wanlin Zhu,[1] Mario Vincenzo Imperatore,[2] Noel Giebink,[2] Susan Trolier-McKinstry,[1] Ismaila Dabo,[1] and Jon-Paul Maria[1]

[1]*The Pennsylvania State University, Department of Materials Science and Engineering, University Park, Pennsylvania 16802, USA*
[2]*The Pennsylvania State University, Department of Electrical Engineering and Computer Science, University Park, Pennsylvania 16802, USA*

(Received 19 December 2020; revised 17 March 2021; accepted 13 April 2021; published 27 April 2021)

This manuscript demonstrates ferroelectricity in B-substituted AlN thin films and a complementary set of first-principles calculations to understand their structure-property relationships. $Al_{1-x}B_xN$ films are grown by dual-cathode reactive magnetron sputtering on (110)W/(001)Al_2O_3 substrates at 300°C at compositions spanning $x = 0$ to $x = 0.20$. X-ray diffraction studies indicate a decrease in both the *c* and *a* lattice parameters with increasing B concentration, resulting in a decrease in unit cell volume and a constant *c*/*a* axial ratio of 1.60 over this composition range. Films with $0.02 \leqslant x \leqslant 0.15$ display ferroelectric switching with remanent polarizations exceeding 125 $\mu C\,cm^{-2}$ while maintaining band gap energies of >5.2 eV. The large band gap allows low frequency hysteresis measurement (200 Hz) with modest leakage contributions. At B concentrations of $x > 0.15$, *c*-axis orientation deteriorates and ferroelectric behavior is degraded. Density-functional theory calculations corroborate the structural observations and provide predictions for the wurtzite *u* parameter, polarization reversal magnitudes, and composition-dependent coercive fields.

DOI: 10.1103/PhysRevMaterials.5.044412

I. INTRODUCTION

AlN has the polar wurtzite structure (space group $P6_3mc$) with a spontaneous polarization parallel its *c* axis, along which pyroelectricity and piezoelectricity are observed. The combination of high mechanical quality factor, reasonable coupling coefficients, high electrical resistivity, high breakdown strength, thermal stability, and low dielectric loss have made it ubiquitous in thin film bulk acoustic wave and microelectromechanical systems devices [1]. Recently, the demands of next-generation communication systems have spurred research into impurity substituted AlN thin films with improved piezoelectric properties. Enhanced AlN thin film piezoelectric properties are achieved in substitutional solid solutions between AlN and a series of transition metal nitrides including ScN [2,3], YN [4], and $Mg_{1-x}Nb_xN$ [5]. Akiyama *et al.* [2] demonstrated that alloying with ScN up to 43 mol% improves the piezoelectric modulus of AlN by up to 400%, as long as the wurtzite structure is preserved. This enhancement is attributed to an increase in ionic bonding character and a structural frustration between wurtzitic and hexagonal polymorphs which soften the potential energy landscape, making the lattice more susceptible to external perturbations like stress or electric fields [6]. Fichtner *et al.* [7] investigated the high-field response of $Al_{1-x}Sc_xN$ thin films and discovered ferroelectric switching with remanent polarizations >100 $\mu C\,cm^{-2}$. Fichtner proposed that a hexagonal BN-like structure is the high-field transition state through which polarization reversal occurs. With increasing Sc concentration, the wurtzite internal parameter *u* (the length of the metal-nitrogen bond along the *c* axis with respect to the *c* parameter) approaches 1/2. Increasing *u* towards 1/2 flattens the AlN puckered hexagonal rings and lowers the energy barrier to traverse the transition state, resulting in a reduction in switching fields with increasing Sc content.

Despite the striking properties achieved in Sc-substituted AlN, modification with semiconducting ScN (band gap, E_g, = 1.58 eV) causes an undesired reduction in the band gap of $Al_{1-x}Sc_xN$ from ~6.1 eV for $x = 0$ to as low as ~2.9 eV for $x = 0.45$; in this composition range the coercive fields approach the breakdown voltage [8–11]. Additionally, Sc is a strategic element which is not optimal for ferroelectric nitride devices produced at scale. In this article, we explore B-substituted AlN as an alternative ferroelectric nitride that contains only complementary metal-oxide-semiconductor (CMOS)-compatible elements and that maintains a large band gap and manageable leakage current in compositions exhibiting robust polarization reversal. Further, current CMOS-compatible ferroelectrics like HfO_2 and $Hf_{1-x}Zr_xO_2$ commonly require high temperature anneals >600 °C to stabilize the ferroelectric phase [12–14]. We demonstrate that highly textured ferroelectric boron-substituted AlN alloys with W metal electrodes can be fabricated at thermal budgets as low as 300°C.

AlN-based alloys of interest for piezoelectric and ferroelectric applications typically employ binary transition metal nitrides as the substituent, many of which possess the rocksalt structure and are semiconductors with indirect band gaps of about 0.5–2 eV [8,15]. First-principles calculation have shown that while both ScN and YN are unstable in the wurtzite phase, they can form a metastable intermediate layered hexagonal phase with an in-plane cation coordination of 3 [16]. On the other hand, BN exists in the layered hexagonal phase under equilibrium conditions where B adopts a threefold coordination in covalently bonded sheets held together by

*Corresponding author: jmhhayden@psu.edu

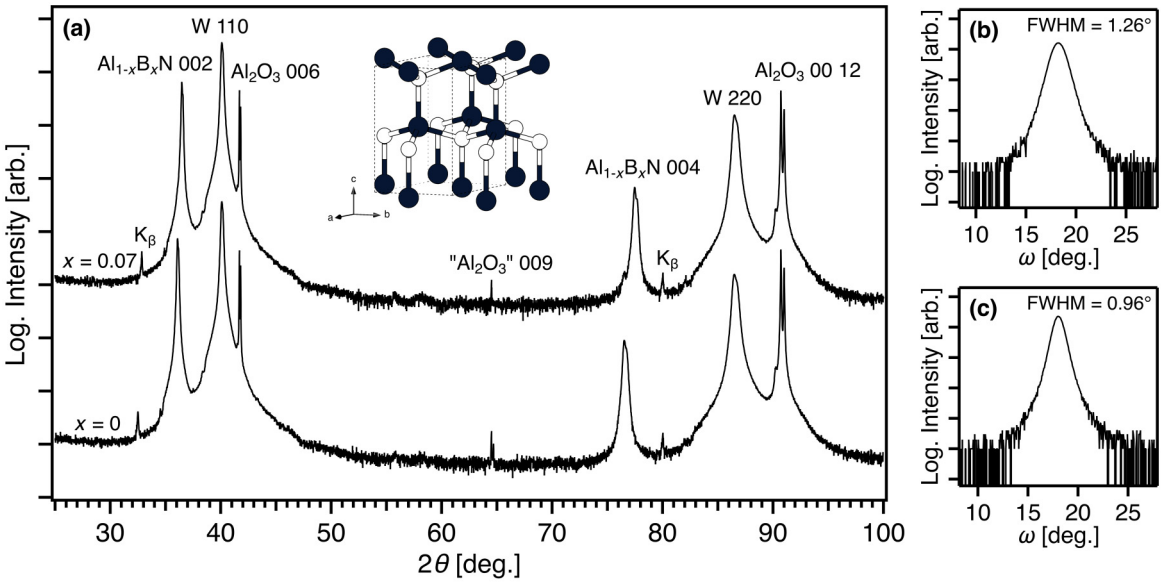

FIG. 1. XRD symmetric θ-2θ (a) and wurtzite-002 rocking curve (b) scans of 500 nm $Al_{0.93}B_{0.07}N$ (top) and AlN (bottom) films prepared on (110)W/(001)Al_2O_3 substrates. The inset drawing depicts the wurtzite crystal structure for AlN.

predominantly van der Waals forces. Since BN has a band gap of 5.2 eV in its hexagonal form and 6.4 eV in its cubic form [17], B modification suggests the possibility for structural softening in AlN without severe band gap reduction.

Herein, we report on the structural, electrical, and optical properties of ferroelectric $Al_{1-x}B_xN$ (AlBN) thin films fabricated using dual-magnetron reactive sputtering. High quality, epitaxial AlBN can be grown at 300°C on W coated *c*-axis Al_2O_3 substrates. Films with as low as 2 mol% BN exhibit robust ferroelectric behavior similar to that observed in the $Al_{1-x}Sc_xN$ (AlScN) system with remanent polarizations larger than 125 μC cm^{-2}. Moreover, AlBN maintains a band gap >4.9 eV throughout the experimentally accessible composition range, allowing for polarization hysteresis measurements at 200 Hz without substantial leakage current contributions.

II. RESULTS AND DISCUSSION

We chose 7 mol% BN as a representative composition with a boron content roughly centered in the accessible wurtzite window. Figure 1(a) shows the x-ray diffraction (XRD) θ-2θ patterns for a 500-nm thick $Al_{0.93}B_{0.07}N$ film on (110)W/(001)Al_2O_3 substrate. For comparison, a pure AlN film grown under similar conditions with the same thickness is also shown. The only reflections present are from the AlBN (00*l*), W (*hh*0), and Al_2O_3(00*l*) planes, indicating that both pure AlN and B-substituted films have the wurtzite structure and exhibit *c*-axis texture. Rocking curves of the $Al_{0.93}B_{0.07}N$ and AlN 002 reflections shown in Figs. 1(b) and 1(c) have full-width-half-maximum (FWHM) values of 1.26° and 0.96° respectively, demonstrating modest out-of-plane crystalline mosaicity in both films.

Nested polarization-electric field (*P*-*E*) measurements of these films are shown in Fig. 2. The film with $x = 0.07$ displays a saturated hysteretic response with nearly ideal boxlike shape, similar to $Al_{1-x}Sc_xN$ films shown by Fichtner *et al.*

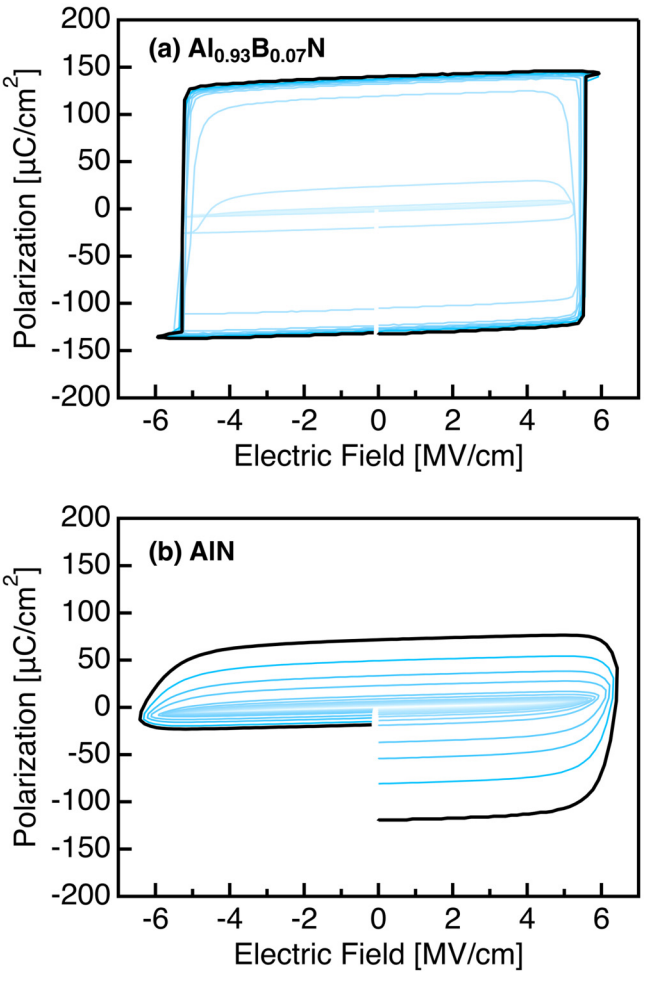

FIG. 2. Room temperature polarization hysteresis for 500 nm $Al_{0.93}B_{0.07}N$ (a) and AlN (b) films measured with a 200 Hz triangular wave. Nested loops are displayed at 0.1 MV cm^{-1} increments.

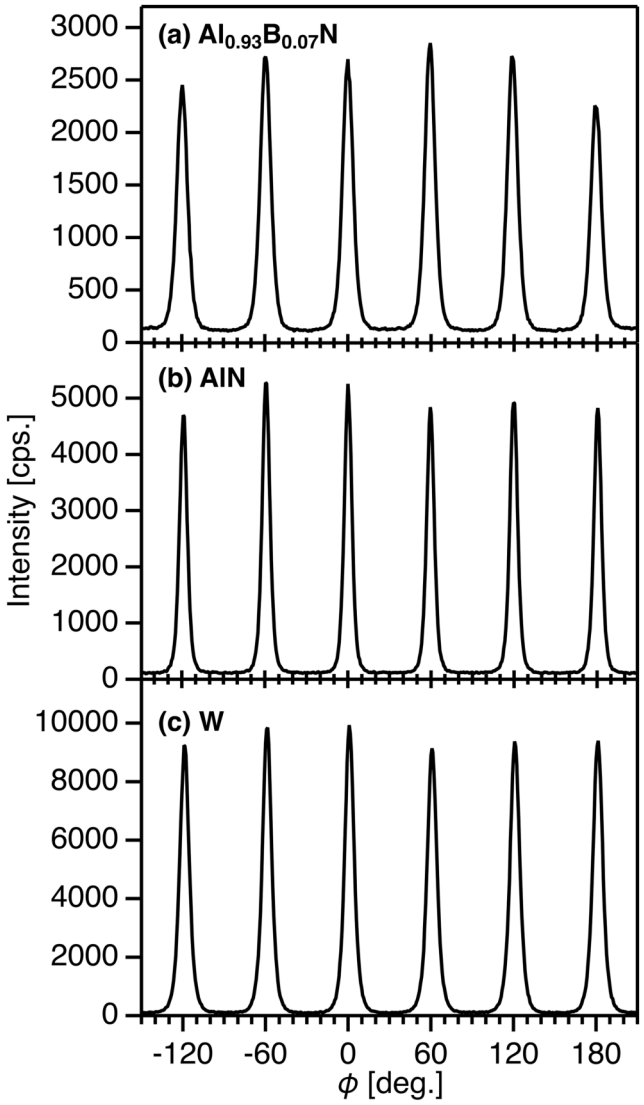

FIG. 3. Skew symmetric φ scans of the $Al_{0.93}B_{0.07}N$ 105 (a), AlN 105 (b), and W 310 reflections.

[7]. The large remanent polarization (P_r) of 136 μC cm^{-2} and coercive field (E_c) of 5.4 MV cm^{-1} agree closely with previous reports [7,18].

For reference, hysteresis measurements of pure AlN films are shown in Fig. 2(b). While there are indications of polarization switching, dc leakage obfuscates our ability to conclude or refute the possibility of ferroelectricity in pure AlN thin films. Similarly ambiguous ferroelectric switching behavior of pure AlN thin films was also reported by Yasuoka *et al.* [18]. It is possible that tuning deposition conditions to either reduce in-plane compressive strain or boost in-plane tensile strain might enable clearer demonstrations of polarization reversal even without boron.

Figure 3 shows azimuthal φ scans of the 105 reflections for $Al_{0.93}B_{0.07}N$ and AlN films and 310 reflection for the W bottom electrode. Each scan shows six diffraction peaks separated by 60°, indicating epitaxial registry of the wurtzite (001) plane to the (110) plane of the W bottom electrode with three possible in-plane orientations for the W layer with respect to the (001) plane of the Al_2O_3 substrate. An averaged FWHM across the six peaks gives an estimated variation in in-plane orientation of 8.9° for $Al_{0.93}B_{0.07}N$, 6.5° for AlN, and 8.0° for W.

To investigate composition-dependent structural modifications that accompany ferroelectric switching in the AlBN solid solution region, in-plane and out-of-plane XRD measurements were performed as a function of B content. Figure 4(a) shows symmetric scans of the 002 reflection for 500-nm-thick AlBN films between $x = 0$ and $x = 0.20$. For the present deposition conditions, 20 mol% BN was the solubility ceiling, higher concentrations were associated with crystallinity diminished to levels no longer interesting. The 002 peak position shifts from 36.08° for pure AlN to 36.89° for $Al_{0.80}B_{0.20}N$. Above 15 mol% BN, peak intensities fall abruptly and rocking curves become broadened, FWHM values for the 002 reflection are shown in Fig. 4(b). It is possible that the reduced B target-to-substrate distances used to produce films with $x = 0.19$ and 0.20 (see experimental methods) causes diminished c-axis crystallinity at these concentrations, but we suspect alloys of this composition introduce a wurtzite phase instability. The averaged $K\alpha_1$ peak position from a pseudo-Voigt fit to the peak profiles for the 002 and 004 reflections was used to estimate the c lattice parameter for AlBN films. Additional skew-symmetric scans of the AlBN 105 reflection were performed to estimate the a lattice parameter using the same treatment. Figure 4(c) shows the measured (filled markers) and calculated (open markers) AlBN c and a lattice parameters as a function of B content; the c/a ratio is shown in Fig. 4(d). Both the c and a lattice parameter decrease monotonically with increasing B content, indicating that alloying AlN with BN results in an overall reduction in unit cell volume. It is probable that the small ionic radius of B compared to Al produces this trend. Since both the c and a parameters decrease at essentially the same rate, the c/a axial ratio is held constant at 1.60 ± 0.01. This result is consistent with the predicted structural trends where c/a does not vary significantly, especially within the experimentally accessible compositional region for AlBN. By contrast, with increasing x, the AlScN c axis shrinks while the basal plane expands, producing a c/a ratio that reduces to nearly 1.3 at $x = 0.46$ [2]. This observation influences the coercive field trends, as discussed below.

Figures 5(a)–5(e) shows polarization hysteresis measurements at 200 Hz for 500 nm AlBN films with $x = 0.00$, 0.02, 0.07, 0.15, 0.19, and 0.20 (the same series shown in Fig. 4) using W top and bottom electrodes. When $0.02 \leqslant x \leqslant 0.15$ polarization hysteresis is fully saturated and P_r decreases slightly with increasing B content [Fig. 5(g)]. At concentrations greater than $x = 0.15$ crystalline fidelity is lost, the maximum polarization is diminished, and the hysteresis loops become less square. At $x = 0.20$, the material is less well oriented (rocking curve FWHM = 3.46°) and has diminished crystalline order (2θ FWHM = 0.29°); the dielectric response is linear up to 5.5 MV cm^{-1}. At this stage, the origin of polarization reduction with increasing B content is not clear, but we speculate that mechanisms associated with steadily increasing crystallographic disorder are responsible. Emerging grain populations with polar axes oriented off-normal are a likely contributing mechanism, as has been

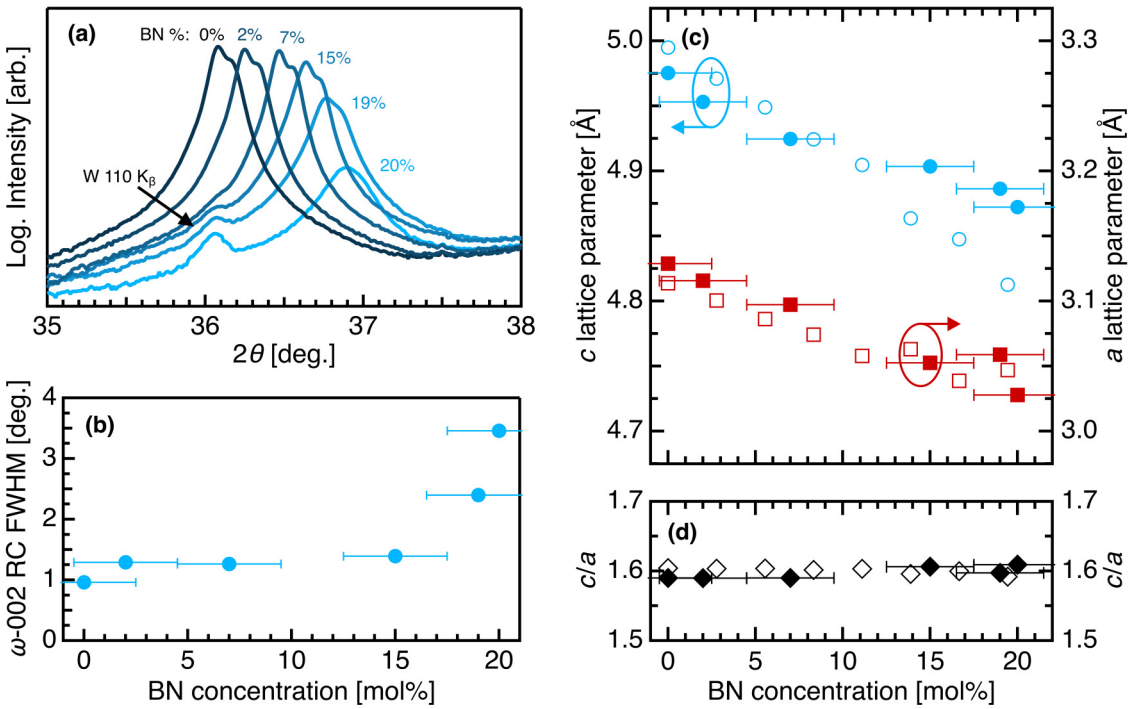

FIG. 4. (a) XRD symmetric θ-2θ scans of the $Al_{1-x}B_xN$ 002 reflection for $x = 0.00, 0.02, 0.07, 0.15, 0.19, 0.20$. (b) Rocking curve FWHM values of the $Al_{1-x}B_xN$ 002 reflection for the same films plotted as a function of B concentration. (c) $Al_{1-x}B_xN$ c and a lattice parameters as a function of B concentration, as determined by in- and out-of-plane XRD measurements (filled markers) and first-principles calculations (open markers). The c/a axial ratio is also shown. Error in the measured lattice parameters is smaller than the size of the markers.

reported in the AlScN system [19]. Additionally, at $x = 0.15$, the x-ray rocking curve nearly maintains its FWHM value, but the peak intensity in 2θ is substantially reduced (about 40%). It is possible that the 2θ intensity reduction occurs because of disorder in $00l$ interplanar spacing, or because of an increased surface fraction of abnormal grains, contributing to the reduction in polarization. The B concentration dependence of E_c is given in Fig. 5(f). Similar to the AlScN system, increasing the substitutional impurity reduces E_c, but the dynamic range is smaller for AlBN than AlScN; over the accessible composition space, E_c falls by 13% and 55% respectively [7].

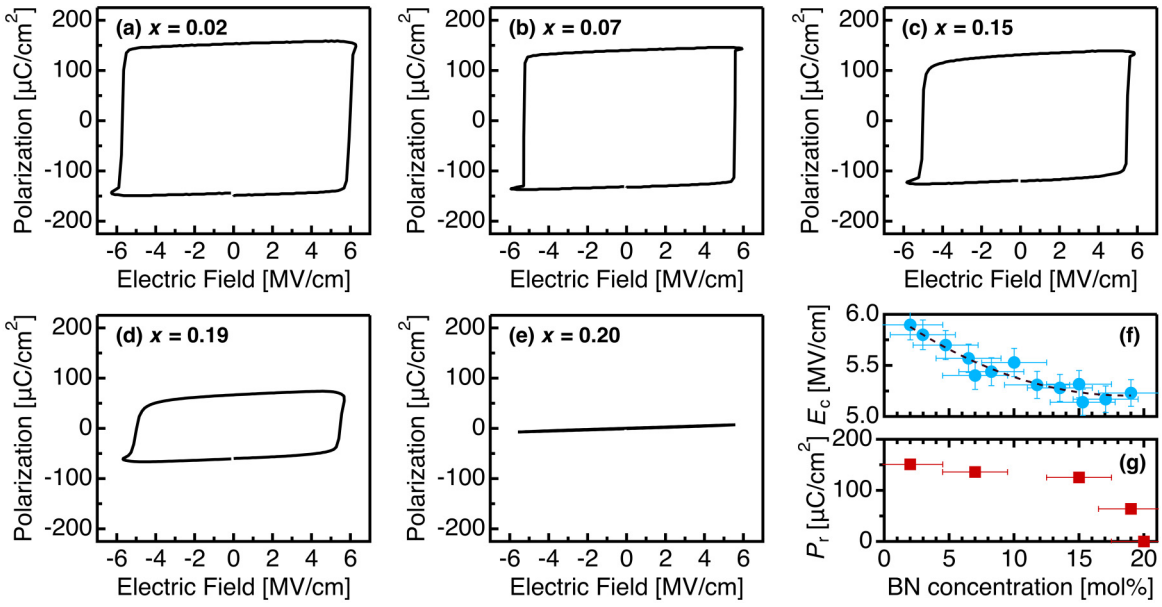

FIG. 5. (a)–(e) Polarization hysteresis for 500 nm $Al_{1-x}B_xN$ films with $x = 0.00, 0.02, 0.07, 0.15, 0.19, 0.20$ measured with a 200 Hz triangular wave. (f) Dependence of coercive field (E_c) on B concentration. Coercive field values are averages of the switching field measured under positive and negative voltage. (g) Dependence of remanent polarization (P_r) on B concentration.

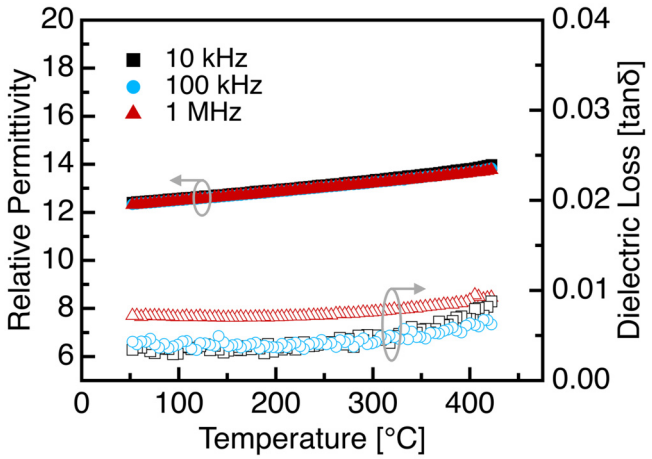

FIG. 6. Temperature dependence of the relative dielectric permittivity and low-field dielectric loss of a 500-nm ferroelectric $Al_{1-x}B_xN$ film with $x = 0.10$. Measurements were performed at 10 kHz, 100 kHz, and 1 MHz with a small signal amplitude of 100 mV. Filled markers represent the permittivity data and open markers the dielectric loss.

Figure 6 gives the temperature dependent small signal dielectric properties of an $Al_{0.90}B_{0.10}N$ film at 10 kHz, 100 kHz, and 1 MHz. At 1 MHz the relative permittivity increases nearly linearly with increasing temperature from about 12 at 50°C to about 14 at 425°C. Between 10 kHz and 1 MHz, there is approximately 2% dispersion for all temperatures. The dielectric loss is low with $\tan(\delta) < 0.01$ throughout the entire temperature range.

Absorption coefficients (α) for AlBN films were determined by ultraviolet-visible reflectance spectroscopy. Band gap energies reported in Fig. 7 were determined from a Tauc plot of $\sqrt{\alpha h\nu}$ versus photon energy, $h\nu$. The gap energy for the pure AlN film is 6.0 eV, consistent with previous reports for thin film and bulk AlN [11,20,21]. The gap energy decreases with increasing B content to a minimum value of 4.9 eV at

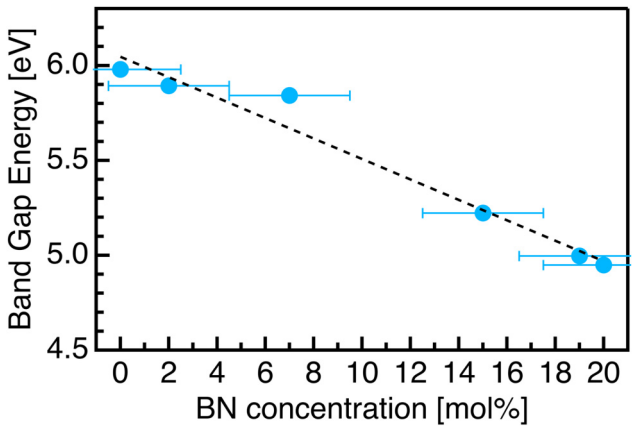

FIG. 7. Band gap energy dependence of AlBN films on B concentration as determined from a Tauc plot using aborption coeffiecients from ultraviolet-visible light reflectance spectroscopy. Error in the measured band gap is smaller than the size of the markers.

$x = 0.20$. Up to $x = 0.07$, $Al_{1-x}B_xN$ films maintain a gap energy of >5.8 eV; the high resistivity of these films is reflected in the shape of the low-frequency hysteresis displayed in Figs. 5(a)–5(c).

Figure 8 shows normal incidence scanning electron micrograph (SEM) images of $Al_{1-x}B_xN$ with varying B content. Films with $x \leqslant 0.15$ have a surface morphology consisting of scattered faceted protuberances surrounded by a smooth matrix of densely packed *c*-axis oriented grains (Zone 2 growth in the revised structure zone model by Anders [22]).

This result is reminiscent of the abnormally oriented grains (AOG) observed in the AlScN system which nucleate at grain boundaries where Sc accumulates in large concentration, rather than at the substrate interface [19]. When $x > 0.15$ the AOG population increases dramatically, and accounts for nearly all surface grains. The polarization-field trace in Fig. 5(e) was collected on the film shown in Fig. 8(f), both corresponding to 20% BN substitution. The film exhibits a linear dielectric response despite withstanding even higher electric fields than films with less B. Although the films could not be switched experimentally, x-ray diffraction shows that a significant fraction of material retains *c*-axis orientation, as such, it is not clear if 20% BN is the ceiling for ferroelectricity, for sustaining orientation stability, or for stabilizing the wurtzite phase. It is possible that 20% BN pushes the structure into the centrosymmetric hexagonal polymorph, or that considerable AOG surface coverage prohibits switching of the underlying *c*-axis oriented material. Additional studies are needed to explore this phase, composition, and film microstructure space.

To complete this preliminary experimental investigation of the structural, dielectric, and optical property spaces available to the AlN-BN solid solution system, we conducted first-principles calculations over a comparable composition range with the intent to relate thermodynamic barriers, atomic displacements, and spontaneous polarizations, which may not be directly accessible experimentally. The computational model, which is further described in the experimental methods section, consists of estimating the coercive fields from the relative enthalpic stabilities of the $Al_{1-x}B_xN$ polymorphs. As shown in Fig. 9(a), the wurtzite phase is thermodynamically stable over the entire composition range ($0 < x < 0.20$), albeit with an energy separation between the two structures that decreases gradually with BN concentrations. Figure 9(b) provides an estimate of the global u parameter (by averaging the fractional longitudinal displacement along the [001] direction for every Al and B atom), which indicates that it is relatively independent of composition. By approximating local atomic charges as Born (differential) effective charges using density-functional perturbation theory [23], spontaneous polarizations can be calculated. The results reported in Fig. 9(c) show a moderate increase in the polarization from 121 $\mu C\,cm^{-2}$ to 128 $\mu C\,cm^{-2}$ as the BN substitution increases from 0% to 20%. In comparison, polarization hysteresis measurements exhibit switchable polarizations between 125 and 150 $\mu C\,cm^{-2}$, in acceptable agreement with first-principles predictions, though the polarization decreases with increasing B concentration. We speculate the opposing trend between experiment and theory is crystalline in origin. In fact, rocking curve measurements demonstrated FWHM increases by a

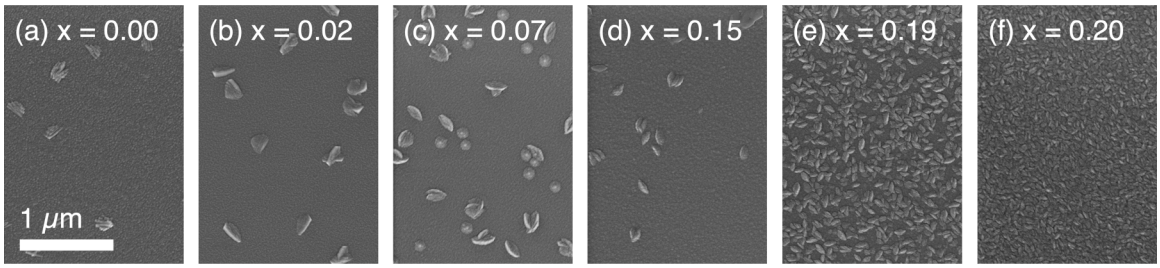

FIG. 8. Normal incidence SEM micrographs of 500 nm $Al_{1-x}B_xN$ films with $x = 0.00, 0.02, 0.07, 0.15, 0.19, 0.20$.

small amount for even low B ($x = 0.02$) substitution. In the entire composition spectrum, density functional theory (DFT) predicts polarization increases by $7\,\mu C\,cm^{-2}$ whereas experimentally polarization decreases by only $\sim 25\,\mu C\,cm^{-2}$ before the precipitous drop in out-of-plane orientation at $x = 0.19$ at which point the polarization is only $\sim 60\,\mu C\,cm^{-2}$. It seems that crystalline defects and alternatively oriented grains are linked to the maximum observed value. Furthermore, it is important to note that we measure and report the remanent polarization which is the quantity that is field re-orientable. It may be that the crystalline polarization is indeed larger, but for reasons associated with microstructure, crystal structure, and point defects, not all can be field reversed. Lastly, the accuracy of the computed polarization may be improved by directly calculating the polarization using accurate (e.g., hybrid) functionals [24].

Finally, Fig. 9(d) shows the coercive field E_c computed as the ratio of the estimated switching barrier height to the polarization per unit cell. Expectedly, since the relative changes in the estimated barrier height [Fig. 9(a)] are more pronounced than for the spontaneous polarization [Fig. 9(c)], they dominate the dependence of the coercive field as a function of B concentration. At $x = 0$, the coercive field is predicted to be $15\,MV\,cm^{-1}$, which is significantly larger than the breakdown strength for AlN. Between $x = 0$ and $x = 0.08$, the coercive field drops sharply to $\sim 7\,MV\,cm^{-1}$. Increasing the B concentration to $x = 0.20$ causes a moderate reduction in the coercive field (to $\sim 6\,MV\,cm^{-1}$), confirming the limited dependency on B content observed experimentally. Calculated coercive fields were in general larger than those measured experimentally for AlBN films, especially at low B concentrations. We attribute this discrepancy to built-in crystalline disorder that inevitably accompanies high energy, kinetically dominated sputtering processes. Defects, off-stoichiometric tendencies, and bombardment induced stresses introduced during film growth are likely contributors to crystalline disorder, resulting in films that differ from the simulated crystal structures. It is important to emphasize that the overarching trend in E_c prediction matches experiment, i.e., it falls with increasing B concentration and with a very modest rate after several percent B. While there are discrepancies in the low B content predictions, the values above $\sim 5\%$ BN offer reasonable agreement. Considering a DFT calculation where $x = 0.027$, only one of the 72 atoms in the supercell is a B, which is essentially an isolated defect. To reduce uncertainties associated with the dilute conditions, the energy barrier calculation was repeated in a 128-atom cell with two substituted B atoms, which is equivalent to $x = 0.031$. This calculation predicts the energy barrier is ~ 0.26 eV which is the same value obtained for an isolated B substitution in the 72-atom cell, so we can speculate that supercell size effects are not predominant. Additionally, it is important to note that predictions do not include temperature effects, nucleation, and growth aspects of the switching process, measurement frequency effects, and the role of defects, all of which could modify E_c. Nonetheless, the general conclusion is clear: B modification to AlN causes a significant reduction in barrier height such that ferroelectric switching becomes possible at low concentrations of boron, while further substitution produces a mostly unchanging barrier height and thus a weak coercive field dependency on B content.

III. CONCLUSIONS

Epitaxial B-substituted AlN thin films were successfully grown on W/Al_2O_3 substrates at 300°C by reactive dual-magnetron sputtering from metallic targets. Films with $0.02 \leqslant x \leqslant 0.15$ displayed ferroelectric switching behavior similar to that reported in the $Al_{1-x}Sc_xN$ system with polarizations larger than $125\,\mu C\,cm^{-2}$ and coercive fields of $>5.0\,MV\,cm^{-1}$. Structural analysis by XRD revealed that the *c* and *a* lattice parameters both decreased with increasing B content, but that the *c*/*a* axial ratio remained the same, resulting in a reduction in unit cell volume. At high B substitution levels of $x \geqslant 0.15$, films showed reduced crystallinity with larger in- and out-of-plane mosaicity, as well as greatly diminished remanent polarization values. Reduction in the switching field observed with increasing B content is attributed to the addition of a substituent with a preferred threefold coordination, though it is conjectured that contraction of the wurtzite basal plane limits the dynamic range of E_c. Notably, addition of an insulating substituent allowed for growth of $Al_{1-x}B_xN$ thin films with band gap energies of >4.9 eV throughout the range of fabricated compositions, resulting in low leakage current contributions to electrical measurements. First-principles calculations indicated a reduction in switching barrier height upon initial B substitution up to $x = 0.08$, allowing for ferroelectric switching before breakdown, but minor reductions in the barrier height for $0.08 \leqslant x \leqslant 0.20$ resulted in a weak coercive field dependence on B content in $Al_{1-x}B_xN$.

IV. EXPERIMENTAL SECTION

Film preparation: Ferroelectric $Al_{1-x}B_xN$ (AlBN) capacitors were prepared on 100-nm well oriented (110) W bottom electrodes (rocking curve FWHM $< 0.6°$) on (001) Al_2O_3 substrates (Jiaozuo TreTrt Materials). Prior to bottom

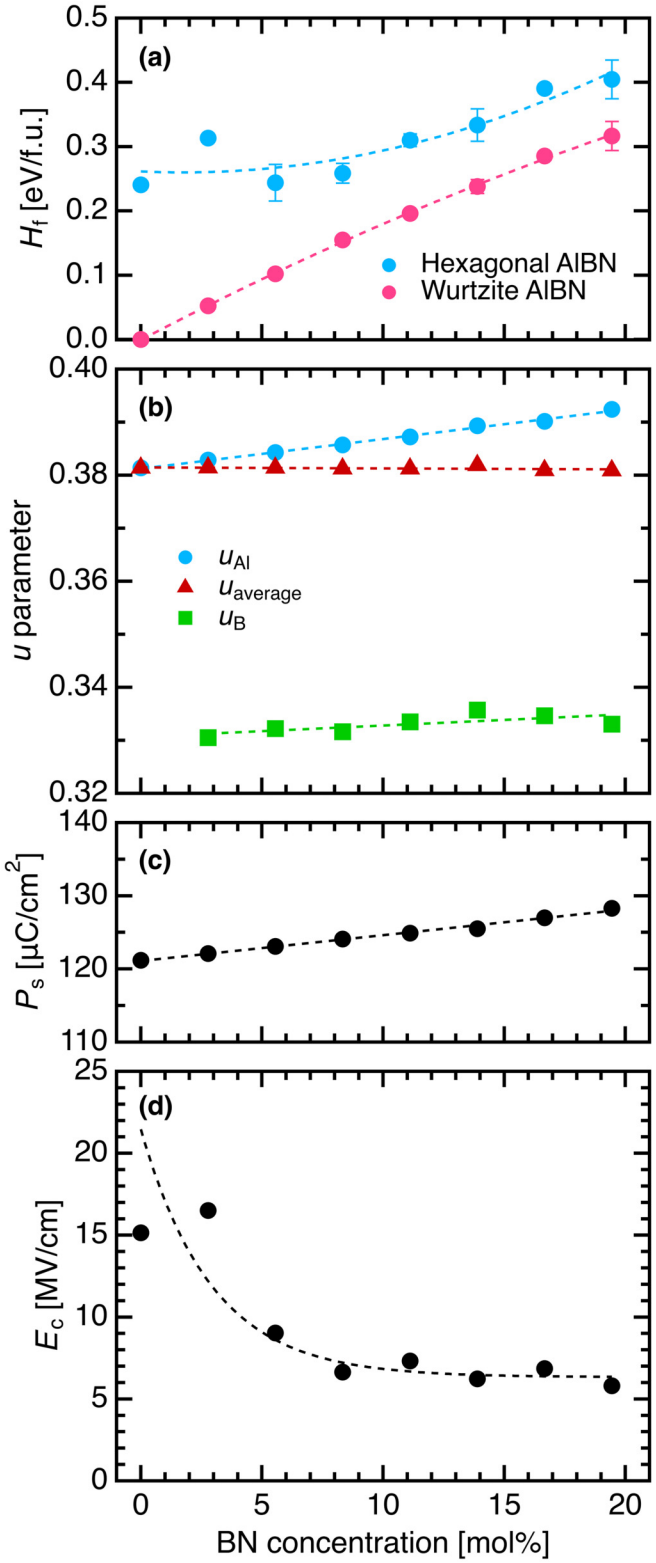

FIG. 9. First-principles predictions of the (a) enthalpies of formation H_f of the hexagonal and wurtzite polymorphs (relative to the wurtzite AlN and hexagonal BN reference phases), (b) wurtzite structural parameter u (referenced to the Al sites, B sites, and as a global average), (c) spontaneous polarization P_s, and (d) coercive field E_c, plotted as a function of B content in $Al_{1-x}B_xN$. (The dashed lines are included as a guide for the eye.)

electrode deposition, substrates were cleaned for 30 s with isopropyl alcohol and methanol on a spin coater at 4000 rpm. The substrate temperature was maintained at 300°C by radiative heating for deposition of the bottom electrode and AlBN layers. 100-nm-W bottom electrodes were deposited by dc sputtering in Ar from a 1 in. W (99.95%, Kurt J. Lesker) target at 5 mTorr, 40 W target power, and 4-cm target-to-substrate distance (TSD). Without breaking vacuum, AlBN films were deposited by reactive pulsed dc sputtering from a 2 in. Al (99.9995%, Kurt J. Lesker) target and rf sputtering from a 2 in. B (99.5%, Plasmaterials) target using MeiVac MAK magnetron sputter sources in a balanced magnetic configuration. The magnetrons are oriented in a sputter-down geometry with a 10-cm TSD and an incident angle of 45° from the substrate normal. AlBN films were sputtered in a mixed nitrogen and argon atmosphere at 1.7 mTorr flowing 10 sccm Ar and 10 sccm N_2. The pulsed dc parameters for the Al source were kept constant at 100 kHz and 1536 ns pulse width with a time averaged power of 200 W. Control over B content in AlBN films was achieved by changing rf power on the B source (e.g., 150 W resulted in 15 mol% BN) for films with $0.00 \leqslant x \leqslant 0.15$. Due to B plasma instability at rf powers greater than 150 W, the B target-to-substrate distance was decreased by 1.6 cm and 2.2 cm for deposition of $Al_{0.81}B_{0.19}N$ and $Al_{0.80}B_{0.20}N$ films, respectively. For electrical characterization, 100 nm W top electrodes with an area of 0.05 mm^2 were deposited at room temperature through a shadow mask with dc sputtering.

Characterization: Film stoichiometry was determined with a Physical Electronics VersaProbe II X-ray photo electron spectroscopy (XPS) instrument equipped an Al $K\alpha$ X-ray source with energy of 1486.6 eV. The photoelectrons were collected by a hemispherical analyzer with a pass energy of 58.7 eV. To eliminate adventitious carbon and native oxide from the surface, all samples were presputtered with a 2-keV Ar^+ beam. To counteract preferential sputtering effects, a stoichiometric AlN film was used as a reference, allowing for a correction factor during data analysis to rectify the Al:N ratio in all films. Spectra were analyzed with the CasaXPS software v2.3.19, data were fit with a combination of Lorentzian asymmetric line shape and Shirley background. High resolution XPS spectra were collected from the N1s, B1s and Al2p electronic shells in order to obtain a better signal-to- noise ratio.

Symmetric XRD $2\theta-\omega$ patterns and rocking curves were measured using Cu radiation from a PANalytical Empyrean diffractometer in Bragg-Brentano geometry. The incident optic was the Bragg-Brentano HD module with 1/8° divergence slit, 1/2° antiscatter slit, and 4-mm beam mask. The diffracted beam optic was the Pixcel3D detector with 0.4 rad Soller slit and 1/4° antiscatter slit. Skew-symmetric $2\theta-\omega$ scans and rotary φ scans of the wurtzite 105 reflection were measured using the same optics. The lattice constants of $Al_{1-x}B_xN$ films were estimated from the $K\alpha_1$ contribution to the 002, 004, and 105 reflections fit with a pseudo-Voigt profile.

P-E field characteristics were measured using a custom-built polarization measurement system using a high voltage amplifier (Trek 2205) with a triangular ac field signal at a frequency of 200 Hz. The temperature dependence of permittivity and dielectric loss of $Al_{1-x}B_xN$ films was measured from 10 kHz to 100 MHz in the temperature range from 50°C

to 425°C using a Keysight 4980 LCR meter with a 100 mV small-signal ac field.

Specular reflectance measurements were carried out in an Agilent Cary 7000 UV-Vis-NIR spectrophotometer equipped with a Universal Measurement Accessory. Spectra were collected in the wavelength range 190–1100 nm with unpolarized light at an incident angle of 6°. The absorption coefficient, α, was extracted from the envelope of the Fabry-Perot oscillations in reflectance (ΔR), which are damped above the band edge according to $\alpha \approx (\Delta R_0 - \Delta R)(1 + R_0)^2/(4dR_0)$, where d is the film thickness and ΔR_0 and R_0 are the Fabry-Perot oscillation amplitude and single interface Fresnel reflectance below the band gap, respectively. The band gap energy was subsequently determined from a Tauc plot of $\sqrt{\alpha h\nu}$ versus photon energy, $h\nu$ (assuming direct allowed transitions [25]), and linearly extrapolating the data to determine its intersection with the abscissa.

$Al_{1-x}B_xN$ surface morphology was studied by SEM using a Zeiss SIGMA VP-FESEM 500 with 2 kV accelerating voltage at a 1.4-mm working distance. To minimize surface charging, prior to imaging, a roughly 3-nm thick W layer was deposited on film surfaces and electrically connected to the mounting slabs with carbon tape.

Computational Methods: Density-functional theory calculations were performed using the Vienna *Ab initio* Simulation Package (VASP) with the projected augmented wave method under the generalized-gradient approximation, following the Perdew-Burke-Ernzerhof (PBE) parameterization of exchange-correlation electronic interactions [26–28]. The parent structure is either wurtzite ($P6_3mc$) w-AlN or hexagonal ($P6_3/mmc$) h-BN. van der Waals interactions are captured at the D3 level, as proposed by Grimme *et al.* [29]. We systematically evaluated how different dispersion corrections affect the relative energies of the reference compounds (AlN and BN). The PBE-D3 method correctly predicts the hexagonal lowest-energy phase of BN, at variance with PBE and PBE-D2. To simulate the experimentally relevant range of compositions ($0 \leqslant x \leqslant 0.20$), 72-atom supercells were constructed. The boron atoms were distributed using the special quasirandom structure generation module of the Alloy Theoretic Automated Toolkit (ATAT) package [30]. Calculations were repeated for three representative random supercells at each boron concentration. The energy cutoff was set to 520 eV and a Γ-centered Monkhorst-Pack grid of $2 \times 2 \times 2$ **k**-point grids was used. The formation enthalpies were calculated as $H_f = E_{w/h,\ Al_{1-x}B_xN} - (1-x)E_{w,AlN} - xE_{h,BN}$, where $E_{w/h,\ Al_{1-x}B_xN}$ is the energy of the B-substituted wurtzite or hexagonal cell, and $E_{w,AlN}$ and $E_{h,BN}$ are the energies of the wurtzite AlN and hexagonal BN phases, respectively. The spontaneous polarization along the c direction of the crystal was calculated as $P_s = \frac{e}{\Omega}\sum_k Z_k \Delta u_k$, where e is the electron charge, Ω is the crystal volume, Z represents the longitudinal diagonal component of the Born effective charge tensor calculated from density-functional perturbation theory [23,31], Δu is the atomic displacement along the c direction, and the sum is carried out over all the ions in the supercell. In defining the longitudinal atomic displacements, we adopt the base of the nitrogen tetrahedra that is perpendicular to the (001) plane in the Wurtzite phase as a reference, as the switching of the Al/B ions across this reference plane is the primary contribution to the observed ferroelectricity. The coercive field was obtained as $E_c \sim \frac{\Delta}{\Omega P_s}$, where Δ is the energy difference between the wurtzite and hexagonal $Al_{1-x}B_xN$ structures.

ACKNOWLEDGMENTS

The authors thank the Defense Advanced Research Projects Agency (DARPA) via Army Research Office (ARO) Grant No. W911NF-20-2-0274, and the Center for Dielectrics and Piezoelectrics (CDP) through National Science Foundation (NSF) Grants No. IIP-1841453 and No. IIP-1841466, for supporting the experimental portions of this work. The first-principles calculations were supported as part of the US Department of Energy, Office of Science, Office of Basic Energy Sciences Energy Frontier Research Centers program under Award No. DE-SC0021118.

[1] M.-A. Dubois and P. Muralt, Properties of aluminum nitride thin films for piezoelectric transducers and microwave filter applications, Appl. Phys. Lett. **74**, 3032 (1999).

[2] M. Akiyama, T. Kamohara, K. Kano, A. Teshigahara, Y. Takeuchi, and N. Kawahara, Enhancement of piezoelectric response in scandium aluminum nitride alloy thin films prepared by dual reactive cosputtering, Adv. Mater. **21**, 593 (2009).

[3] S. Fichtner, T. Reimer, S. Chemnitz, F. Lofink, and B. Wagner, Stress controlled pulsed direct current Co-sputtered $Al_{1-x}Sc_xN$ as piezoelectric phase for micromechanical sensor applications, APL Mater. **3**, 116102 (2015).

[4] P. M. Mayrhofer, H. Riedl, H. Euchner, M. Stöger-Pollach, P. H. Mayrhofer, A. Bittner, and U. Schmid, Microstructure and piezoelectric response of $Y_xAl_{1-x}N$ thin films, Acta Mater. **100**, 81 (2015).

[5] M. Uehara, H. Shigemoto, Y. Fujio, T. Nagase, Y. Aida, K. Umeda, and M. Akiyama, Giant increase in piezoelectric coefficient of aln by Mg-Nb simultaneous addition and multiple chemical states of Nb, Appl. Phys. Lett. **111**, 112901 (2017).

[6] R. E. Newnham and G. R. Ruschau, Smart electroceramics, J. Am. Ceram. Soc. **74**, 463 (1991).

[7] S. Fichtner, N. Wolff, F. Lofink, L. Kienle, and B. Wagner, AlScN: A III-V Semiconductor based ferroelectric, J. Appl. Phys. **125**, 114103 (2019).

[8] C. Stampfl, W. Mannstadt, R. Asahi, and A. J. Freeman, Electronic structure and physical properties of early transition metal mononitrides: Density-functional theory LDA, GGA, and screened-exchange LDA FLAPW calculations, Phys. Rev. B **63**, 155106 (2001).

[9] R. Deng, S. R. Evans, and D. Gall, Bandgap in $Al_{1-x}Sc_xN$, Appl. Phys. Lett. **102**, 112103 (2013).

[10] J. Yang, M. M. Cao, Y. D. Li, and Y. G. Chen, Structure and optical properties of $Al_{1-x}Sc_xN$ thin films, Key Eng. Mater. **537**, 140 (2013).

[11] M. Baeumler, Y. Lu, N. Kurz, L. Kirste, M. Prescher, T. Christoph, J. Wagner, A. Žukauskaitė, and O. Ambacher, Optical constants and band gap of wurtzite $Al_{1-x}Sc_xN/Al_2O_3$ prepared by magnetron sputter epitaxy for scandium concentrations up to x = 0.41, J. Appl. Phys. **126**, 045715 (2019).

[12] T. S. Böscke, J. Müller, D. Bräuhaus, U. Schröder, and U. Böttger, Ferroelectricity in hafnium oxide thin films, Appl. Phys. Lett. **99**, 102903 (2011).

[13] J. Müller, T. S. Böscke, U. Schröder, S. Mueller, D. Bräuhaus, U. Böttger, L. Frey, and T. Mikolajick, Ferroelectricity in simple binary ZrO_2 and HfO_2, Nano Lett. **12**, 4318 (2012).

[14] S. Mueller, J. Mueller, A. Singh, S. Riedel, J. Sundqvist, U. Schroeder, and T. Mikolajick, Incipient ferroelectricity in al-doped HfO_2 thin films, Adv. Funct. Mater. **22**, 2412 (2012).

[15] B. Eck, R. Dronskowski, M. Takahashi, and S. Kikkawa, Theoretical calculations on the structures, electronic and magnetic properties of binary 3d transition metal nitrides, J. Mater. Chem. **9**, 1527 (1999).

[16] P. Guan, C. Wang, and T. Yu, Electronic structure and physical properties of stable and metastable phases in YN: Density-functional theory calculations, Sci. Bull. **53**, 3131 (2008).

[17] S. N. Mohammad, Electrical characteristics of thin film cubic boron nitride, Solid State Electron. **46**, 589 (2002).

[18] S. Yasuoka, T. Shimizu, A. Tateyama, M. Uehara, H. Yamada, M. Akiyama, Y. Hiranaga, Y. Cho, and H. Funakubo, Effects of deposition conditions on the ferroelectric properties of $(Al_{1-x}Sc_x)N$ thin films, J. Appl. Phys. **128**, 114103 (2020).

[19] C. S. Sandu, F. Parsapour, S. Mertin, V. Pashchenko, R. Matloub, T. LaGrange, B. Heinz, and P. Muralt, Abnormal grain growth in AlScN thin films induced by complexion formation at crystallite interfaces, Phys. Status Solidi A **216**, 1800569 (2019).

[20] Q. Guo and A. Yoshida, Temperature dependence of band Gap change in InN and AlN, Jpn. J. Appl. Phys. **33**, 2453 (1994).

[21] M. Feneberg, R. A. R. Leute, B. Neuschl, K. Thonke, and M. Bickermann, High-excitation and high-resolution photoluminescence spectra of bulk AlN, Phys. Rev. B **82**, 075208 (2010).

[22] A. Anders, A structure zone diagram including plasma-based deposition and ion etching, Thin Solid Films **518**, 4087 (2010).

[23] S. Baroni, S. de Gironcoli, A. Dal Corso, and P. Giannozzi, Phonons and related crystal properties from density-functional perturbation theory, Rev. Mod. Phys. **73**, 515 (2001).

[24] J. Heyd, G. E. Scuseria, and M. Ernzerhof, Hybrid functionals based on a screened coulomb potential, J. Chem. Phys. **118**, 8207 (2003).

[25] W. M. Yim, E. J. Stofko, P. J. Zanzucchi, J. I. Pankove, M. Ettenberg, and S. L. Gilbert, Epitaxially grown AlN and its optical band gap, J. Appl. Phys. **44**, 292 (1973).

[26] J. P. Perdew, K. Burke, and M. Ernzerhof, Generalized Gradient Approximation Made Simple, Phys. Rev. Lett. **77**, 3865 (1996).

[27] G. Kresse and J. Furthmüller, Efficient iterative schemes for *ab initio* total-energy calculations using a plane-wave basis set, Phys. Rev. B **54**, 11169 (1996).

[28] G. Kresse and D. Joubert, From ultrasoft pseudopotentials to the projector augmented-wave method, Phys. Rev. B **59**, 1758 (1999).

[29] S. Grimme, J. Antony, S. Ehrlich, and H. Krieg, A consistent and accurate *ab initio* parametrization of density functional dispersion correction (DFT-D) for the 94 elements H-Pu, J. Chem. Phys. **132**, 154104 (2010).

[30] A. van de Walle, M. Asta, and G. Ceder, The alloy theoretic automated toolkit: A user guide, Calphad **26**, 539 (2002).

[31] M. Noor-A-Alam, O. Z. Olszewski, and M. Nolan, Ferroelectricity and large piezoelectric response of AlN/ScN superlattice, ACS Appl. Mater. Interfaces **11**, 20482 (2019).